

Single crystal growth and characterization of 166-type magnetic kagome metals

Huangyu Wu(吴黄宇), Jinjin Liu(刘锦锦), Yongkai Li(李永恺), Peng Zhu(朱鹏), Liu Yang(杨柳), Fuhong Chen(陈富红), Deng Hu(胡灯), and Zhiwei Wang(王秩伟)

Citation: Chin. Phys. B, 2024, 33 (**9**): 098101. DOI: 10.1088/1674-1056/ad553b
Journal homepage: http://cpb.iphy.ac.cn; http://iopscience.iop.org/cpb

What follows is a list of articles you may be interested in

Single crystal growth and transport properties of narrow-bandgap semiconductor RhP_2

De-Sheng Wu(吴德胜), Ping Zheng(郑萍), and Jian-Lin Luo(雒建林)
Chin. Phys. B, 2024, 33 (**8**): 088101. DOI: 10.1088/1674-1056/ad4cd5

A new transition metal diphosphide α-MoP_2 synthesized by a high-temperature and high-pressure technique

Xiaolei Liu(刘晓磊), Zhenhai Yu(于振海), Jianfu Li(李建福), Zhenzhen Xu(徐真真), Chunyin Zhou(周春银), Zhaohui Dong(董朝辉), Lili Zhang(张丽丽), Xia Wang(王霞), Na Yu(余娜), Zhiqiang Zou(邹志强),Xiaoli Wang(王晓丽), and Yanfeng Guo(郭艳峰)
Chin. Phys. B, 2023, 32 (**1**): 018102. DOI: 10.1088/1674-1056/ac633d

Super deformability and thermoelectricity of bulk γ-InSe single crystals

Bin Zhang(张斌), Hong Wu(吴宏), Kunling Peng(彭坤岭), Xingchen Shen(沈星辰), Xiangnan Gong(公祥南), Sikang Zheng(郑思康), Xu Lu(卢旭), Guoyu Wang(王国玉), and Xiaoyuan Zhou(周小元)
Chin. Phys. B, 2021, 30 (**7**): 078101. DOI: 10.1088/1674-1056/abf133

Regulation mechanism of catalyst structure on diamond crystal morphology under HPHT process

Ya-Dong Li(李亚东), Yong-Shan Cheng(程永珊), Meng-Jie Su(宿梦洁), Qi-Fu Ran(冉启甫), Chun-Xiao Wang(王春晓), Hong-An Ma(马红安), Chao Fang(房超), Liang-Chao Chen(陈良超)
Chin. Phys. B, 2020, 29 (**7**): 078101. DOI: 10.1088/1674-1056/ab90e8

Influence of vacuum degree on growth of Bi_2Te_3 single crystal

Tang Yan-Kun (唐雁坤), Zhao Wen-Juan (赵文娟), Zhu Hua-Qiang (朱化强), Huang Yong-Chao (黄勇潮), Cao Wei-Wei (曹伟伟), Yang Qian (杨倩), Yao Xiao-Yan (姚晓燕), Zhai Ya (翟亚), Dong Shuai (董帅)
Chin. Phys. B, 2015, 24 (**7**): 078101. DOI: 10.1088/1674-1056/24/7/078101

DATA PAPER

Single crystal growth and characterization of 166-type magnetic kagome metals

Huangyu Wu(吴黄宇)[1,2], Jinjin Liu(刘锦锦)[1,2], Yongkai Li(李永恺)[1,2,4], Peng Zhu(朱鹏)[1,2], Liu Yang(杨柳)[1,2], Fuhong Chen(陈富红)[1,2], Deng Hu(胡灯)[1,2], and Zhiwei Wang(王秩伟)[1,2,3,4,†]

[1] *Centre for Quantum Physics, Key Laboratory of Advanced Optoelectronic Quantum Architecture and Measurement (MOE), School of Physics, Beijing Institute of Technology, Beijing* 100081, *China*

[2] *Beijing Key Laboratory of Nanophotonics and Ultrafine Optoelectronic Systems, Beijing Institute of Technology, Beijing* 100081, *China*

[3] *Beijing Institute of Technology, Zhuhai* 519000, *China*

[4] *Material Science Center, Yangtze Delta Region Academy of Beijing Institute of Technology, Jiaxing* 314011, *China*

(Received 23 May 2024; revised manuscript received 5 June 2024; accepted manuscript online 7 June 2024)

Kagome magnets were predicted to be a good platform to investigate correlated topology band structure, Chern quantum phase, and geometrical frustration due to their unique lattice geometry. Here we reported single crystal growth of 166-type kagome magnetic materials, including $HfMn_6Sn_6$, $ZrMn_6Sn_6$, $GdMn_6Sn_6$ and GdV_6Sn_6, by using the flux method with Sn as the flux. Among them, $HfMn_6Sn_6$ and $ZrMn_6Sn_6$ single crystals were grown for the first time. X-ray diffraction measurements reveal that all four samples crystallize in $HfFe_6Ge_6$-type hexagonal structure with space group *P6/mmm*. All samples show metallic behavior from temperature dependence of resistivity measurements, and the dominant carrier is hole, except for GdV_6Sn_6 which is electron dominated. All samples have magnetic order with different transition temperatures, $HfMn_6Sn_6$, $ZrMn_6Sn_6$ and GdV_6Sn_6 are antiferromagnetic with T_N of 541 K, 466 K and 4 K respectively, while $GdMn_6Sn_6$ is ferrimagnetic with the critical temperature of about 470 K. This study will enrich the research platform of magnetic kagome materials and help explore the novel quantum phenomena in these interesting materials. The dataset of specific crystal structure parameters for $HfMn_6Sn_6$ are available in Science Data Bank, with the link https://doi.org/10.57760/sciencedb.j00113.00120.

Keywords: kagome metal, single crystal growth, crystal structure, physical property

PACS: 81.10.–h, 71.55.Ak, 75.47.–m **DOI:** 10.1088/1674-1056/ad553b

1. Introduction

The kagome lattice[1] consists of triangles with shared angles, and has a special honeycomb structure, which allows kagome structured materials to have both linearly dispersive Dirac bands and non-dispersive flat bands. In recent decades, variety of novel quantum effects have been discovered in kagome lattice systems, such as giant anomalous Hall effect, long-range ferromagnetic ordering, superconductivity and quantum spin liquids.[2,3] For example, the quasi-two-dimensional kagome materials AV_3Sb_5 (A = K, Rb, Cs) have received much attention due to their outstanding properties, including superconductivity, charge density wave (CDW), time-reversal symmetry breaking, anomalous Hall or anomalous Nernst effects.[4,5] The magnetic kagome materials Fe_3Sn_2, Mn_3Sn, $Co_3Sn_2S_2$ with a giant anomalous Hall effect have been reported and extensively studied. The presence of flat bands in Fe_3Sn_2 induces local spin polarization, long-range ferromagnetic sequence, anisotropic magnetic tunability, and orbital magneto-nonlinear anomalous Hall effect.[6–9] Mn_3Sn is reported to be the first antiferromagnet with zero field anomalous Hall effect, the small magnetization is considered to be conducive for the generation of spin Hall effect. It provides a good platform to elucidate the role of magnetism on spin Hall effect, and promotes the development of antiferromagnetic spintronics.[10,11] Additionally, the magnetic Weyl semimetal $Co_3Sn_2S_2$ is the first material in which large anomalous Hall angles coexist with anomalous Hall effects.[12–14] Therefore, magnetic kagome lattice materials provide an ideal platform for studying the interplay between Dirac band, flat band and magnetism.

In addition to the magnetic kagome materials mentioned above, $TbMn_6Sn_6$, a new 166-type material with an independent defect-free kagome lattice was reported to be conducive to the generation of Chern gap Dirac fermions, anomalous Hall effect, etc. In 2021, a series of topological kagome magnets RMn_6Sn_6 (R = Gd–Tm, Lu) were found to have quantum transport properties similar to the quantum limit Chern magnet $TbMn_6Sn_6$.[15–18] Actually, there are various series of kagome systems that are known as the 166-type compounds, with the general formula RT_6X_6 (R = rare earth elements; T = Mn, V, Fe; X = Sn, Ge). Due to the different sizes of the atoms, some compounds crystallize to a fully ordered $HfFe_6Ge_6$-type structure, and others form a disordered YCo_6Ge_6-type or $SmMn_6Sn_6$-type structure.[19,20] For the former structure,

†Corresponding author. E-mail: zhiweiwang@bit.edu.cn

© 2024 Chinese Physical Society and IOP Publishing Ltd

R atoms form the hexagonal layer and the transition metal *T* atoms form the kagome layer. Compounds of this structure have complex magnetic and electronic properties. For example, there is an antiferromagnetic helical magnetic structure and competing magnetic phases in YMn_6Sn_6.[21] And there exhibits large anomalous Hall effect in $LiMn_6Sn_6$[22] and $HoMn_6Sn_6$.[23] More recently, the pressure-tuned magnetic transition temperature (T_m) observed in both compounds GdV_6Sn_6 and TbV_6Sn_6 exhibits a turning point at the critical pressure P_c, accompanied with a sign reversal in the anomalous Hall effect.[24] Due to the novel physical properties of 166-type compounds, many efforts have been put to deeply exploring new physics and their origins.

In this paper, we report the crystal growth and physical properties of 166-type kagome metal. By using Sn as flux, we successfully synthesize $HfMn_6Sn_6$, $ZrMn_6Sn_6$, $GdMn_6Sn_6$, GdV_6Sn_6 single crystals. Their structures are confirmed as $HfFe_6Ge_6$-type. Electrical transport and magnetic properties measurements reveal that $HfMn_6Sn_6$ and $ZrMn_6Sn_6$ are high-temperature antiferromagnetic metals, and GdV_6Sn_6 is also an antiferromagnetic metal but with a quite lower critical temperature. On the contrary, $GdMn_6Sn_6$ is a ferrimagnetic metal with the critical temperature as high as 470 K. We believe these high-quality crystals will provide a foundation for spin storage and sensor applications in the future.[25–28]

2. Methods

2.1. Crystal growth

High quality single crystals of $HfMn_6Sn_6$, $ZrMn_6Sn_6$, $GdMn_6Sn_6$, GdV_6Sn_6 were prepared by using the flux method with Sn as the flux. The starting elements of Hf (powder, 99%)/Zr (powder, 99.9%)/Gd (block, 99.9%), Mn (block, 99.8%)/V (block, 99.5%), and Sn (grain, 99.999%) were mixed with the molar ratio of 1:6:10–30. The mixtures were placed into an aluminum crucible covered with quartz cotton, then sealed in an evacuated quartz tube (inner diameter 11 mm, base pressure lower than 2×10^{-4} Pa). The tubes were heated to 1273 K–1373 K and hold for 24 h, followed by cooling down to 873 K slowly, at which the quartz tubes were put into a centrifuge to remove the flux. We would like to point out that the cooling procedure of growth for $ZrMn_6Sn_6$ is a bit different from others, we should cool fast in the early stage of cooling and then slowly in order to get larger crystals. It is worth noting that the flux can be scraped off with a scalpel and polished with abrasive paper if there was still some flux remaining on the surface of the sample after centrifugation, and the typical size is about 2 mm × 2 mm, as shown in the insets of Fig. 2.

2.2. Characterizations and measurements

The crystal structure was characterized by x-ray diffraction which was performed on the D8 Advance X (Bruker, Germany) x-ray diffractometer equipped with Cu-K_α radiation. Single crystal x-ray for crystallographic analysis was taken from a Bruker D8 QUEST diffractometer equipped with the APEX III software, and the structure was solved and refined by using the SHELXTL software package to get the detailed structure information. The chemical composition of the single crystals was analyzed by energy-dispersive spectroscopy (EDS) equipped on a scanning electron microscope (SEM, JEOL SM-7500F, Japan). Electrical transport measurements were carried out on a physical property measurement system (PPMS, Quantum Design, USA) with the temperature from 300 K to 1.8 K and the external magnetic fields from −11 T to 11 T. The longitudinal resistivity (ρ_{xx}) and Hall resistivity (ρ_{yx}) were measured by using the six-terminal configuration, so that the signals of ρ_{xx} and ρ_{yx} can be taken simultaneously. Before transport measurement, the single crystal was cut into rectangular strips. The contacts were prepared by using gold wires attached with silver glue that was cured at room temperature. Magnetization measurements with temperature below room temperature were carried out using a Quantum Design magnetic property measurement system (MPMS-III), and magnetization measurements with temperature above room temperature were carried out using a vibrating sample magnetometer (VSM Lake shore 7404 series).

3. Results and discussion

3.1. Crystal structure and chemical composition

XRD measurements were performed to check the crystal structures of the as-grown single crystal samples, the results are shown in Fig. 1(b). Only (00*l*) peaks were observed, which can easily be indexed by the space group *P6/mmm* based on the hexagonal $HfFe_6Ge_6$-type structure. The lattice parameter of *c* was calculated and listed in Table 3. The full width at half maximum (FWHM) of (004) peak for all samples is less than 0.07°, the sharp diffraction peak indicates that the good crystallinity of all single crystals. In order to get detailed structure information, we performed single crystal x-ray measurement on $HfMn_6Sn_6$ single crystal and resolved the structure by using the SHELXTL software package, as illustrated in Fig. 1(a). It is found that the kagome layer formed from Mn atom is sandwiched by two layers of Hf and Sn atoms along *c*-axis direction. More detailed crystallographic information is shown in Tables 1 and 2 (see more details in the supplementary material (SM) in HTML format). In order to check the chemical composition and element distribution of the single crystals, EDS was performed on the above four single crystals, as shown in Fig. 2. It is obvious that the corresponding three elements are detected in each sample and no other additional peaks show up. The composition of *R*:*T*:Sn is almost close to 1:6:6. Actually, we checked different positions on

each sample during measurement and found that the composition is basically the same within the instrument error, indicating uniformity of sample composition.

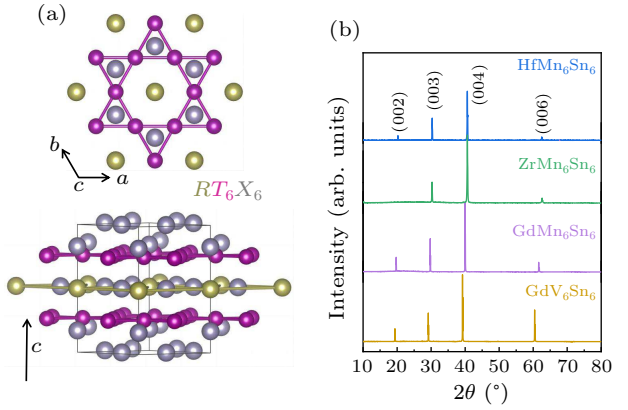


Fig. 1. (a) Schematic crystal structure of RT_6X_6 (R = Hf, Zr, Gd, T = Mn, V, X = Sn) with T atoms shown in pink, R atoms in yellow and X atoms in gray. (b) XRD patterns of single crystal samples with only (00l) peaks.

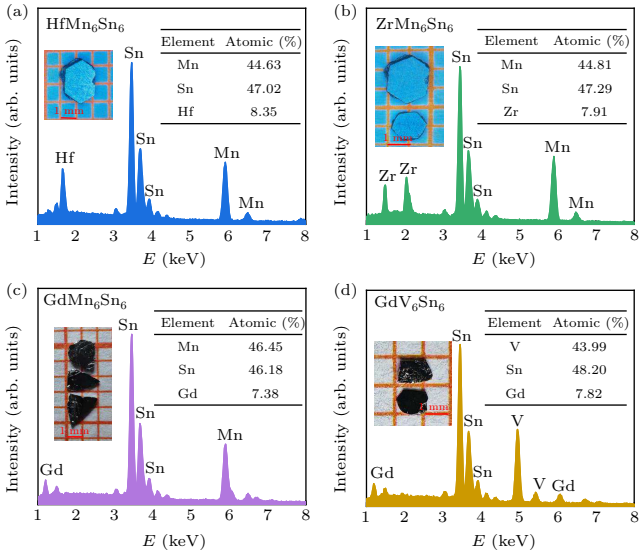


Fig. 2. EDS spectra results of single crystal samples. The inset of each panel shows a photograph of the crystal and composition.

Table 1. Crystallographic data of $HfMn_6Sn_6$.

Empirical formula	$HfMn_6Sn_6$
Formula weight (g/mol)	1220.26
Temperature (K)	273
Crystal system	hexagonal
Space group	$P6/mmm$
Unit cell dimensions	
a (Å)	5.4321(9)
b (Å)	5.4321(9)
c (Å)	8.949(2)
α (°)	90
β (°)	90
γ (°)	120
Volume (Å^3)	228.69(9)
ρ_{calc} (g/cm^3)	8.861
Z	1
μMo $K\alpha$ (mm^{-1})	35.237
R_1; ωR_2 ($I > 2\delta(I)$)	0.0365; 0.0869

Table 2. Atomic coordinates and equivalent isotropic displacement parameters for $HfMn_6Sn_6$.

Atom	Wyck.	Site sys.	Occ.	x/a	y/b	z/c	U_{eq} (Å^2)
Hf	1b	$6/mmm$	1	0	0	0.5	0.0213(7)
Sn1	2e	$6mm$	1	0.0	0.0	0.1703(2)	0.124(6)
Sn2	2c	$-6m2$	1	1/3	2/3	0	0.0113(6)
Sn3	2d	$-6m2$	1	2/3	1/3	0.5	0.0130(6)
Mn	6i	$2mm$	1	0.5	0	0.2536(2)	0.0102(7)

3.2. Transport properties

The temperature dependence of longitudinal resistivity for $HfMn_6Sn_6$, $ZrMn_6Sn_6$, $GdMn_6Sn_6$ and GdV_6Sn_6 crystals is presented in Fig. 3. We can clearly see that the resistivity decreases as the temperature is cooled from 300 K down to 2 K, indicating metallic behaviors for all samples. No obvious transition was observed. The low temperature resistivity data were fit to the formula $\rho_{xx}(T) = \rho(0) + AT + BT^2$ below 100 K, the resulting fits are shown as red curves in each panel in Fig. 3. We found that the resistivity of $GdMn_6Sn_6$ and GdV_6Sn_6 follows the conventional Fermi-liquid $\rho \propto T^2$ behavior. However, $\rho(T)$ of $ZrMn_6Sn_6$ depends linearly on the temperature and $HfMn_6Sn_6$ shows a sum of linear and T^2 dependence, which are likely non-Fermi liquid behaviors. The residual resistivity $\rho(0)$ as well as the parameters of A and B for all four samples were obtained and listed in Table 3. $ZrMn_6Sn_6$ has the largest $\rho(0)$ of 75.99 μΩ·cm, and $GdMn_6Sn_6$ has the smallest one of 2.59 μΩ·cm. The residual resistivity ratio ($RRR = \rho_{xx}$ (300 K)/$\rho(0)$) was calculated to be 1.65, 3.41, 18.8 and 15.3 for $HfMn_6Sn_6$, $ZrMn_6Sn_6$, $GdMn_6Sn_6$ and GdV_6Sn_6, respectively. The higher RRR values in $GdMn_6Sn_6$ and GdV_6Sn_6 suggest that the scattering effects in these two samples are weaker than those in the other two.

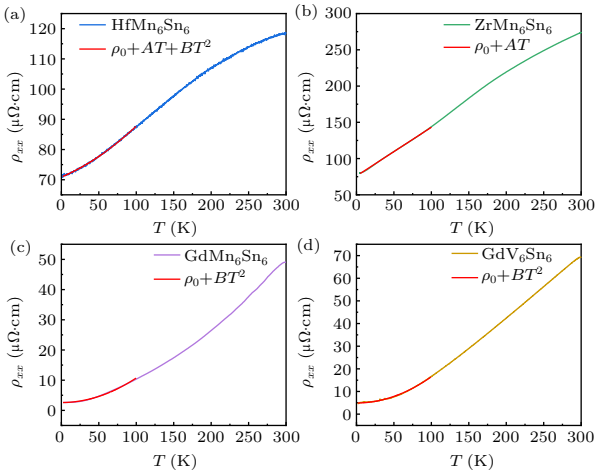


Fig. 3. Temperature dependence of longitudinal resistivity of the four crystals measured at zero magnetic field. The red curves show an effective parametrization of the data below 100 K via the equation $\rho = \rho_0 + AT + BT^2$.

The magnetic field dependence of Hall resistivity was measured at 2 K, as presented in Fig. 4. The $\rho_{yx}(B)$ curves for $HfMn_6Sn_6$ and $GdMn_6Sn_6$ exhibit almost linear behavior with the magnetic field varying. Meanwhile, the slopes

of the curves are positive, indicating the existence of hole-dominant carrier (p type). The carrier density p was calculated to be approximately 1.28×10^{21} cm^{-3} for $HfMn_6Sn_6$ and 1.67×10^{22} cm^{-3} for $GdMn_6Sn_6$. The $\rho_{yx}(B)$ data of GdV_6Sn_6 and $ZrMn_6Sn_6$ are not linear, which suggest the existence of two or more carrier types. GdV_6Sn_6 can be fitted well with the two-band model with the equation

$$R_{xy} = \frac{B}{e} \cdot \frac{\left(n_e\mu_e^2 + n_h\mu_h^2\right) + B^2\mu_e^2\mu_h^2\left(n_e + n_h\right)}{\left(|n_e|\,\mu_e + |n_h|\,\mu_h\right)^2 + B^2\mu_e^2\mu_h^2\left(n_e + n_h\right)^2}, \quad (1)$$

where n_i and μ_i ($i = e, h$) are the carrier concentration and mobility. The two-band fitting gives $n_e = 2.591 \times 10^{21}$ cm^{-3}, $\mu_e = 2068.3$ cm^2·V^{-1}·s^{-1}, $n_h = 1.095 \times 10^{20}$ cm^{-3}, $\mu_h = 442.9$ cm^2·V^{-1}·s^{-1}. This nonlinear Hall resistivity was also reported by Ishikawa *et al.*, where they contributed this nonlinear behavior to the presence of multiple carriers from first-principles calculation.[29] The $\rho_{yx}(B)$ curve of $ZrMn_6Sn_6$ exhibits S-shaped feature, and we tried to fit it with the two-band model, however, the refinement did not converge. This is possibly due to the presence of multiple carriers. Therefore, here we tentatively estimate the carrier concentration from the linear fit at low field region, the result is shown in Table 3.

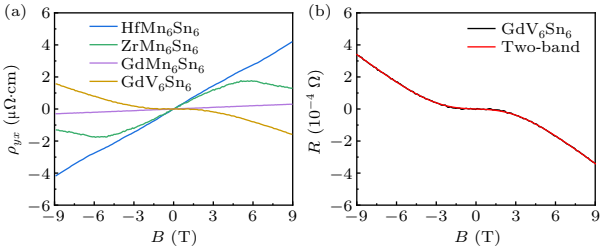


Fig. 4. (a) The field dependence of Hall resistivity (ρ_{yx}) of $HfMn_6Sn_6$, $GdMn_6Sn_6$, GdV_6Sn_6 and $ZrMn_6Sn_6$ measured at 2 K. (b) Two-band fitting for the $\rho_{yx}(B)$ of GdV_6Sn_6.

Table 3. Lattice parameter c, residual resistivity ρ_0, A, B, *RRR*, and carrier concentration of samples.

Sample	c (Å)	ρ_0 (μΩ·cm)	A (μΩ·cm·K^{-1})	B (μΩ·cm·K^{-2})	*RRR*	p (cm^{-3})	n (cm^{-3})
$HfMn_6Sn_6$	8.949(2)	70.89	0.1038	6.49×10^{-4}	1.65	1.28×10^{21}	0
$ZrMn_6Sn_6$	8.973(1)	75.99	0.6720	–	3.41	$\sim 10^{21}$	0
$GdMn_6Sn_6$	9.009(5)	2.59	–	8.14×10^{-4}	18.8	1.67×10^{22}	0
GdV_6Sn_6	9.176(5)	4.92	–	1.16×10^{-3}	15.3	1.1×10^{20}	2.59×10^{21}

3.3. Magnetic properties

$HfMn_6Sn_6$ and $ZrMn_6Sn_6$ polycrystals were reported to be antiferromagnetic with the Néel temperature (T_N) above room temperature by Mazet *et al.*[30] For this sake, we measured the temperature dependence of the magnetization under zero-field-cooling (ZFC) condition with magnetic field parallel to the *ab*-plane of these two single crystals. For the ZFC measurements, the sample was mounted in zero magnetic field at 300 K. And then the *M*–*T* data were collected with increasing temperature under an applied magnetic field of 1 T. As presented in Fig. 5(a), we can clearly see that $HfMn_6Sn_6$ and $ZrMn_6Sn_6$ show antiferromagnetic transition with $T_N \approx 541$ K and $T_N \approx 466$ K, respectively, which was determined by the peak of the derivative of magnetization $dM(T)/dT$. Here the T_N is lower than that in the polycrystals.[30] This may be caused by sample differences and applied magnetic fields. In polycrystal powders, the grain size is usually smaller than our single crystals, also there are lots of grain boundaries in the polycrystalline samples, which will affect the T_N. Besides, the applied magnetic field may be another reason, here we applied a magnetic field of 1 T, whereas in the polycrystalline sample, the applied magnetic field was 0.5 T.[30] The *M*–*T* data of $ZrMn_6Sn_6$ and $HfMn_6Sn_6$ show upturns in the low temperature range, which is somewhat similar to that reported in $ErMn_6Sn_6$.[31] It may be related to the complex magnetic structure in this material. From Fig. 5(d), no hysteresis loop is observed, and the magnetization does not get saturated even at the magnetic field of 11 T. The *M*–*H* curve of $ZrMn_6Sn_6$ shows a nonlinear behavior. This nonlinear behavior appears in some antiferromagnetic materials, such as the antiferromagnetic material $Y_{0.5}Fe_3Sn_3$ reported by Yang Liu *et al.*[32] As the external magnetic field increases, the magnetic moment direction of the sample rotates along the direction of the external magnetic field.

The temperature dependence of magnetization for $GdMn_6Sn_6$ was measured under ZFC conditions with a magnetic field applied parallel to the *ab* plane, as shown in Fig. 5(b). The magnetization curve begins to rise suddenly at about 470 K, indicating a magnetic transition. Figure 5(e) depicts the isothermal magnetization curve of $GdMn_6Sn_6$ at 300 K. The compound is magnetized spontaneously under an external magnetic field parallel to the *ab* plane, and quickly reaches saturation at a very low field, consistent with that reported by Kimura *et al.*,[33] where they claimed a ferrimagnetic transition, and the magnetic moments of Gd-sublattice and Mn-sublattice were antiparallel. A clear hysteresis was observed, suggesting a ferrimagnetic state, as seen in the inset of Fig. 5(e), and the coercive filed H_c is about 15 Oe.

Figure 5(c) presents the temperature dependence of magnetic susceptibility for GdV_6Sn_6 with a magnetic field of 1 kOe applied parallel to the *ab* plane. It is obvious that there is an antiferromagnetic transition at $T_N = 4$ K. The Curie–Weiss fit

$$\frac{M}{H} = \frac{C}{T + \theta} \quad (2)$$

yields $C = 8.33$ emu·mol^{-1}·Oe^{-1}·K^{-1} and $\theta = 9.98$ K, where

C and θ are the Curie constant and Curie–Weiss temperature, respectively. The effective magnetic moment $\mu_{\rm eff}$ can be calculated to be $8.17\mu_{\rm B}$ by using $\mu_{\rm eff} = \sqrt{8C/n}\mu_{\rm B}$, which is very close to $8.1\mu_{\rm B}$ calculated for $Gd^{3+}(4f^7)$ ions when $S = 7/2$.[34] There is no hysteresis in M–H curve, as shown in Fig. 5(f). However, the M–H curve at 2 K shows a saturation behavior, this saturation behavior is similar to that reported by Lee *et al.*[34]

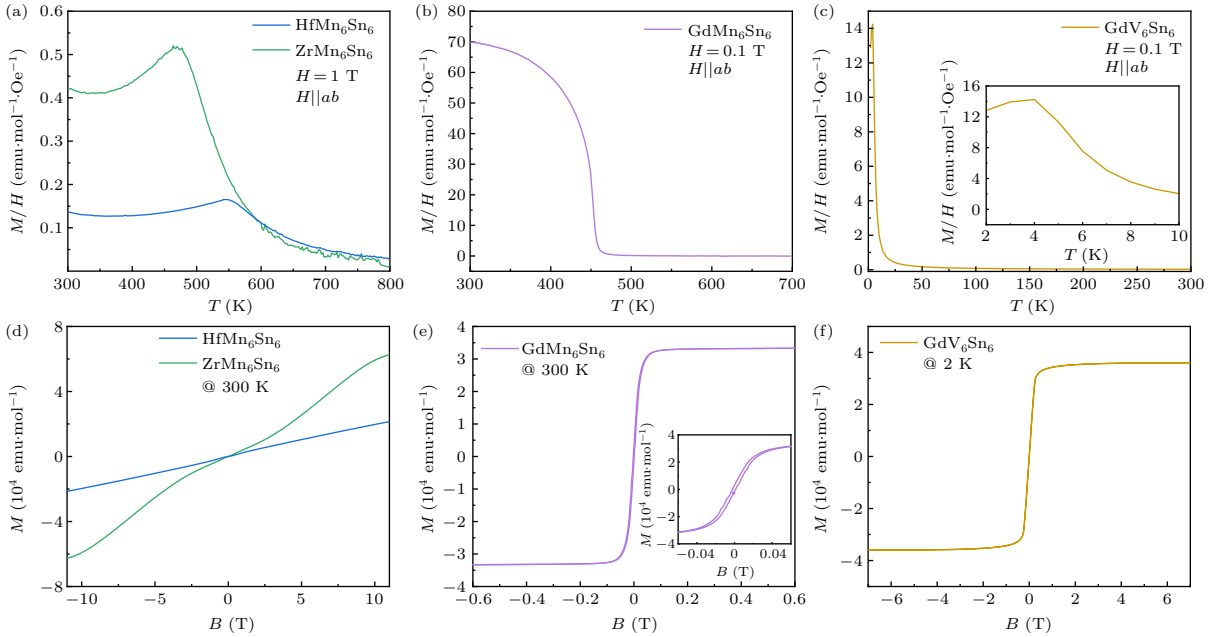


Fig. 5. (a)–(c) The temperature dependence of ZFC magnetization with the applied field paralleling to *ab* plane. The inset of panel (c) shows the magnetization at lower temperature. (d)–(f) Field dependence of magnetization. The inset of panel (e) shows the M–H curve at lower field and a loop can be clearly observed.

4. Conclusion

In summary, we have successfully synthesized $HfMn_6Sn_6$, $ZrMn_6Sn_6$, $GdMn_6Sn_6$ and GdV_6Sn_6 single crystals by using the flux method with Sn as the flux. XRD analysis confirmed that the single crystal crystallized in $P6/mmm$ hexagonal structure. All samples exhibited metallic behavior from the temperature dependence of resistivity measurements. $GdMn_6Sn_6$ and GdV_6Sn_6 showed conventional Fermi-liquid behavior while the other two likely showed a non-fermi liquid behavior. From the magnetic field dependent and temperature-dependent magnetization, we found that $HfMn_6Sn_6$ and $ZrMn_6Sn_6$ were antiferromagnetic with $T_{\rm N}$ above 541 K and 466 K, respectively; $GdMn_6Sn_6$ was ferrimagnetic with the critical temperature of about 470 K, and GdV_6Sn_6 was low-temperature antiferromagnetic with $T_{\rm N}$ about 4 K. Moreover, $HfMn_6Sn_6$ and $ZrMn_6Sn_6$ were very stable in air, and we expect they could have potential application in excellent memory components and future spintronics.

Data availability statement

The data that support the findings of this study are openly available in Science Data Bank at the following link https://doi.org/10.57760/sciencedb.j00113.00120

Acknowledgments

Project supported by the Beijing Natural Science Foundation (Grant No. Z210006), the National Key Research and Development Program of China (Grant Nos. 2022YFA1403400 and 2020YFA0308800), and the Beijing National Laboratory for Condensed Matter Physics (Grant No. 2023BNLCMPKF007). We would like to thank the Synergetic Extreme Condition User Facility (SECUF) for the support of the high temperature magnetic property measurements.

References

[1] Syozi I 1951 *Theor. Phys* **6** 306
[2] Yin J X, Lian B and Hasan M Z 2022 *Nature* **612** 647
[3] Neupert T, Denner M M, Yin J X, Thomale R and Hasan M Z 2022 *Nat. Phys.* **18** 137
[4] Jiang K, Wu T, Yin J X, Wang Z Y, Hasan M Z, Wilson S D, Chen X H and Hu J P 2023 *Natl. Sci. Rev.* **10** nwac199
[5] Nguyen T and Li M D 2022 *J. Appl. Phys.* **131** 060901
[6] Lin Z Y, Choi J H, Zhang Q, Qin W, Yi S H, Wang P D, Li L, Wang Y F, Zhang H, Sun Z, Wei L M, Zhang S B, Guo T F, Lu Q Y, Cho J H, Zeng C G and Zhang Z Y 2018 *Phys. Rev. Lett.* **121** 096401
[7] Yin J X, Zhang S S, Li H, *et al.* 2018 *Nature* **562** 91
[8] Kida T, Fenner L A, Dee A A, Terasaki I, Hagiwara M and Wills A S 2011 *J. Phys.: Condes. Matter.* **23** 112205
[9] Wang L J Y, Zhu J J, Chen H Y, Wang H, Liu J J, Huang Y X, Jiang B Y, Zhao J J, Shi H J, Tian G, Wang H Y, Yao Y G, Yu D P, Wang Z W, Xiao C, Yang S A and Wu X S 2024 *Phys. Rev. Lett.* **132** 106601
[10] Nakatsuji S, Kiyohara N and Higo T 2015 *Nature* **527** 212
[11] Kimata M, Chen H, Kondou K, Sugimoto S, Muduli P K, Ikhlas M, Omori Y, Tomita T, MacDonald A H, Nakatsuji S and Otani Y 2019 *Nature* **565** 627

[12] Liu E K, Sun Y, Kumar N, *et al*. 2018 *Nat. Phys.* **14** 1125

[13] Wang Q, Xu Y F, Lou R, Liu Z H, Li M, Huang Y B, Shen D W, Weng H M, Wang S C and Lei H H 2018 *Nat. Commun.* **9** 3681

[14] Liu D F, Liang A J, Liu E K, Xu Q N, Li Y W, Chen C, Pei D, Shi W J, Mo S K, Dudin P, Kim T, Cacho C, Li G, Sun Y, Yang L X, Liu Z K, Parkin S S P, Felser C and Chen Y L 2019 *Science* **365** 1282

[15] Yin J X, Ma W L, Cochran T A, *et al*. 2020 *Nature* **583** 533

[16] Gao L L, Shen S W, Wang Q, Shi W J, Zhao Y, Li C H, Cao W Z, Pei C Y, Ge J Y, Li G, Li J, Chen Y L, Yan S C and Qi Y P 2021 *Appl. Phys. Lett.* **119** 096401

[17] Zhang H D, Koo J, Xu C Q, Sretenovic M, Yan B H and Ke X L 2022 *Nat. Commun.* **13** 1091

[18] Ma W L, Xu X T, Yin J X, Yang H, Zhou H B, Cheng Z J, Huang Y Q, Qu Z, Wang F, Hasan M Z and Jia S 2021 *Phys. Rev. Lett.* **126** 246602

[19] El Idrissi B C, Venturini G and Malaman B 1991 *Mater. Res. Bull.* **26** 1331

[20] Venturini G 2006 *Z. Krist-cryst Mater.* **221** 511

[21] Ghimire N J, Dally R L, Poudel L, Jones D C, Michel D, Magar N T, Bleuel M, McGuire M A, Jiang J S, Mitchell J F, Lynn J W and Mazin I I 2020 *Sci. Adv.* **6** eabe2680

[22] Chen D, Le C C, Fu C G, Lin H C, Schnelle W, Sun Y and Felser C 2021 *Phys. Rev. B* **103** 144410

[23] Zeng H, Yu G, Luo X H, Chen C C, Fang C S, Ma S C, Mo Z J, Shen J, Yuan M and Zhong Z C 2022 *J. Alloys Compd.* **899** 163356

[24] Kong X M, Tao Z C, Zhang R, Xia W, Chen X, Pei C Y, Ying T P, Qi Y P, Guo Y F, Yang X F and Li S Y 2024 *Chin. Phys. Lett* **41** 047503

[25] Grzybowski M J, Wadley P, Edmonds K W, Campion R P, Dybko K, Majewicz M, Gallagher B L, Sawicki M and Dietl T 2019 *AIP Adv.* **9** 115101

[26] Zhuravlev I A, Adhikari A and Belashchenko K D 2018 *Appl. Phys. Lett.* **113** 162404

[27] Jungwirth T, Marti X, Wadley P and Wunderlich J 2016 *Nat. Nanotechnol.* **11** 231

[28] Wadley P, Howells B, Zelezny J, *et al*. 2016 *Science* **351** 587

[29] Ishikawa H, Yajima T, Kawamura M, Mitamura H and Kindo K 2021 *J. Phys. Soc. Jpn.* **90** 124704

[30] Mazet T, Welter R and Malaman B 1999 *J. Alloys Compd.* **284** 54

[31] Clatterbuck D M and Gschneidner K A 1999 *J. Magn. Magn. Mater.* **207** 78

[32] Liu Y, Lyu M, Liu J Y, Zhang S, Yang J Y, Du Z W, Wang B B, Wei H X and Liu E K 2023 *Chin. Phys. Lett* **40** 047102

[33] Kimura S, Matsuo A, Yoshii S, Kindo K, Zhang L, Brück E, Buschow K H J, de Boer F R, Lefèvre C and Venturini G 2006 *J. Alloys Compd.* **408** 169

[34] Lee J and Mun E 2022 *Phys. Rev. Mater.* **6** 083401